

Pairing-induced motion of source and inert particles driven by surface tension

Hiroaki Ishikawa,¹ Yuki Koyano,² Hiroyuki Kitahata,¹ and Yutaka Sumino^{3,4,*}

¹*Department of Physics, Chiba University, 1-33 Yayoi-cho, Inage-ku, Chiba 263-8522, Japan*

²*Department of Physics, Graduate School of Science, Tohoku University,
6-3, Aoba, Aramaki, Aoba-ku, Sendai 980-8578, Japan*

³*Department of Applied Physics, Faculty of Science Division I,
Tokyo University of Science, 6-3-1 Nijuku, Katsushika-ku, Tokyo 125-8585, Japan*

⁴*WaTUS and DCIS, Research Institute for Science & Technology,
Tokyo University of Science, 6-3-1 Nijuku, Katsushika-ku, Tokyo 125-8585, Japan*

(Dated: November 26, 2021)

We experimentally and theoretically investigate systems with a pair of source and inert particles that interacts through the concentration field. The experimental system comprises a camphor disk as the source particle and a metal washer as the inert particle. Both are floated on a polyethylene glycol (PEG) aqueous solution at various concentrations, where the PEG modifies the viscosity of the aqueous phase. The particles form a pair owing to the attractive lateral capillary force. As the camphor disk spreads surface-active molecules at the aqueous surface, the camphor disk and metal washer move together, driven by the surface tension gradient. The washer is situated in the front of the camphor disk, keeping the distance constant during their motion, which we call a pairing-induced motion. The pairing-induced motion exhibited a transition between circular and straight motions as the PEG concentration in the aqueous phase changed. Numerical calculations using a model that considers forces caused by the surface tension gradient and lateral capillary interaction reproduced the observed transition in the pairing-induced motion. Moreover, this transition agrees with the result of the linear stability analysis on the reduced dynamical system obtained by the expansion with respect to the particle velocity. Our results reveal that the effect of the particle velocity cannot be overlooked to describe the interaction through the concentration field.

I. INTRODUCTION

In nonequilibrium systems, a particle can spontaneously move by consuming free energy, and this is known as a self-propelled particle. The mechanism of such a spontaneous motion of a single particle has been intensively studied [1–5], in addition to their collective behavior [6–11]. Recently, self-propelled particles that interact through a concentration field have attracted attentions as an analog for chemotactic motions of living organisms, e.g., *Dictyostelium* [12] and *E. coli* [13]. In an actual biological situation, the system of interest possesses macroscopic dynamics due to several species interacting within the system [14]. As a pioneering theoretical work, Canalejo et al. reported the active phase separation in the multiparticle system of binary species [15]. In their model, the dynamics of concentration field is adiabatically eliminated. Thus, the particles interact through the concentration fields in an instantaneous manner. However, the concentration field can have their own spatio-temporal dynamics, such as diffusion and chemical reaction, which may alter the characteristics of the particle motion. In fact, the concentration field and the particle position are introduced as independent variables in the model for the camphor disk motion on water [16–19]. This model can show the self-propulsion through spontaneous symmetry breaking owing to the dynamics of the concentration field. Therefore, we investigate the

systems with multiple types of particles coupled with the concentration field having their own dynamics. In the present study, we focus on a simple system that comprises a pair of source and inert particles, both of which are driven by a common concentration field.

In our experiment, we use a camphor disk and metal washer as the source and inert particles, respectively, at the surface of a polyethylene glycol (PEG) aqueous solution. From the camphor disk floating at the surface of the aqueous solution, camphor molecules are continuously spread to the aqueous surface, and then, they are sublimated to the air phase. A consequent spatial gradient of surface tension drives the camphor disk and metal washer [20–28]. The floating metal washer distorts the surface, which causes the attractive lateral capillary force between the camphor disk and metal washer [29]. Owing to the surface tension gradient and attractive capillary force, the camphor disk and metal washer exhibit the motion with a constant mutual distance, a pairing-induced motion. The PEG concentration in the aqueous phase was varied as a control parameter, which changes the viscosity of the aqueous phase. We observed the transition between circular and straight motions as the PEG concentration in the aqueous phase changed. Moreover, we constructed a mathematical model consisting of the reaction-diffusion equation for the surface-active molecules and equations of motion for the source and inert particles. Furthermore, numerical results exhibit the transition from the straight to circular pairing-induced motion. This transition is analytically explained based on the bifurcation theory.

* ysumino@rs.tus.ac.jp

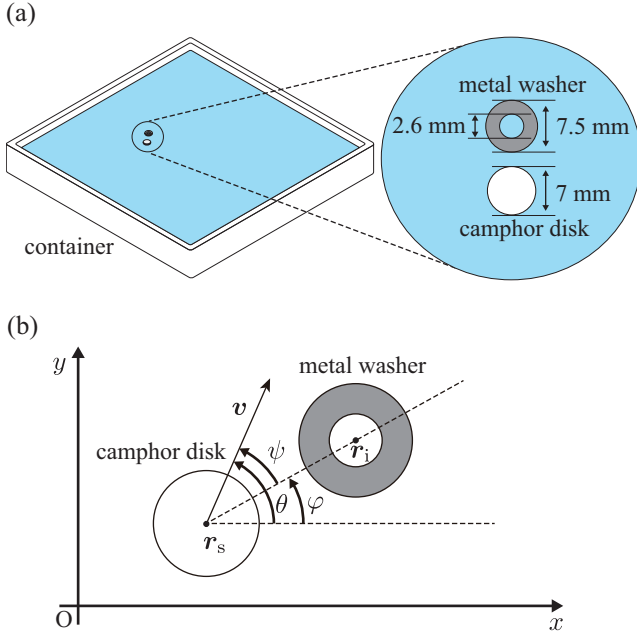


FIG. 1. (a) Experimental setup. A camphor disk and a metal washer were floated at the surface of the PEG aqueous solution in a square-shaped container (245 mm \times 245 mm \times 25 mm). (b) Definition of the variables obtained from the experimental results.

II. EXPERIMENTS

Camphor and PEG 6000 were obtained from Fuji-film Wako Pure Chemical (Osaka, Japan). A stainless washer (diameter 7.5 mm) was obtained from Ohsato (Tokyo, Japan). Water was purified with the Millipore Milli-Q system (Merck, Darmstadt, Germany). A camphor disk (diameter 7 mm) was prepared using a pellet press die set and a compression molding (Pike technologies, Madison, USA). 400 ml of PEG aqueous solution with the concentration of C was poured into a square-shaped polystyrene container (245 mm \times 245 mm \times 25 mm). The shadows of the camphor disk and metal washer at the aqueous surface were recorded from below using a digital CMOS video camera (DMK37BUX273, The Imaging Source, Bremen, Germany) at 10 fps. The experiments were conducted at 25 ± 2 °C, and the captured images were analyzed using ImageJ [30].

We put the metal washer at the PEG aqueous surface and then put the camphor disk. The weight of the metal washer was appropriately chosen, so that it could float at the aqueous surface in spite of the density reversal. They got close to each other owing to the attractive lateral capillary force. After a few seconds, they started a pairing-induced motion, in which the metal washer was in the front side and the camphor disk was in the rear side. Here, the time $t = 0$ was defined as when the pairing-induced motion started. As shown in Figs. 2(a) and (b), they exhibited the circular and straight motions for lower

and higher PEG concentrations, respectively.

For the quantitative discussion on the pairing-induced motion, we measured the centers of mass (COMs) of the camphor disk \mathbf{r}_s^j and the metal washer \mathbf{r}_i^j at time $t = t^j$. First, we calculated the curvature of the camphor disk trajectory to elucidate the transition between the circular and straight motions. In detail, we obtained the velocity $\mathbf{v}^j = (\mathbf{r}_s^{j+1} - \mathbf{r}_s^j)/\Delta t$, where $\Delta t = t^{j+1} - t^j = 0.1$ s. Then, we obtained the angular velocity $\omega^j = (\theta^j - \theta^{j-1})/\Delta t$, where θ^j was calculated by the relation $\mathbf{v}^j = v^j(\cos \theta^j \mathbf{e}_x + \sin \theta^j \mathbf{e}_y)$, where $v^j > 0$. Here, \mathbf{e}_x and \mathbf{e}_y are unit vectors in the x - and y -directions, respectively. φ^j is the angle of the vector of $\mathbf{r}_s^j - \mathbf{r}_i^j$ from the x -axis, and the drift angle is defined as $\psi^j = \theta^j - \varphi^j$. From ω^j and v^j , the unsigned curvature (the absolute value of the curvature) $\kappa^j = \kappa(t^j)$ was obtained as $\kappa^j = 2|\omega^j|/(v^j + v^{j-1})$. $\bar{\kappa}$ was defined as the mean value of κ over the observation time.

The drift angle ψ and angular velocity ω of the camphor disk were fluctuated around a certain finite value during the circular motion (Fig. 2(c)), while both were close to zero during the straight motion (Fig. 2(d)). The observed spikes in Fig. 2(d) correspond to sharp turns at the container wall. When the particles exhibited the circular motion, the drift angle ψ had the opposite sign to the angular velocity ω (Fig. 2(e)). It implies that the metal washer rotated at a smaller radius than the camphor disk. When the particles exhibited straight motion, the drift angle ψ and angular velocity ω were almost zero (Fig. 2(f)). Figure 2(g) shows the distribution p of the unsigned curvature κ at each PEG concentration C . When C was between 0.001 g/L and 0.1 g/L, the distribution had a long tail, indicating the trajectory is circular. In contrast, when C was between 1.0 and 50 g/L, the distribution exhibited a strong peak at $\kappa = 0$, which reflects a straight trajectory. These changes in the distribution of κ with C are summarized by averaging $\bar{\kappa}$ (Fig. 2(h)). The plot captures a sharp decrease in $\bar{\kappa}$ when C increases, indicating the transition. The lower PEG concentration corresponds to smaller viscosity; therefore, the straight motion exhibited the transition to the circular motion as the viscosity decreased.

III. NUMERICAL SIMULATIONS

We construct a mathematical model to discuss the pairing-induced motion of the camphor disk and metal washer floating at the aqueous surface observed in the experimental system. In our model, the camphor disk and metal washer are regarded as the source and inert particles, respectively. We consider the time development of the source particle position $\mathbf{r}_s(t)$, the inert particle position $\mathbf{r}_i(t)$, and the concentration field $u(\mathbf{r}, t)$ in the two-dimensional space, which corresponds to the aqueous surface.

The dynamics for the concentration field is described

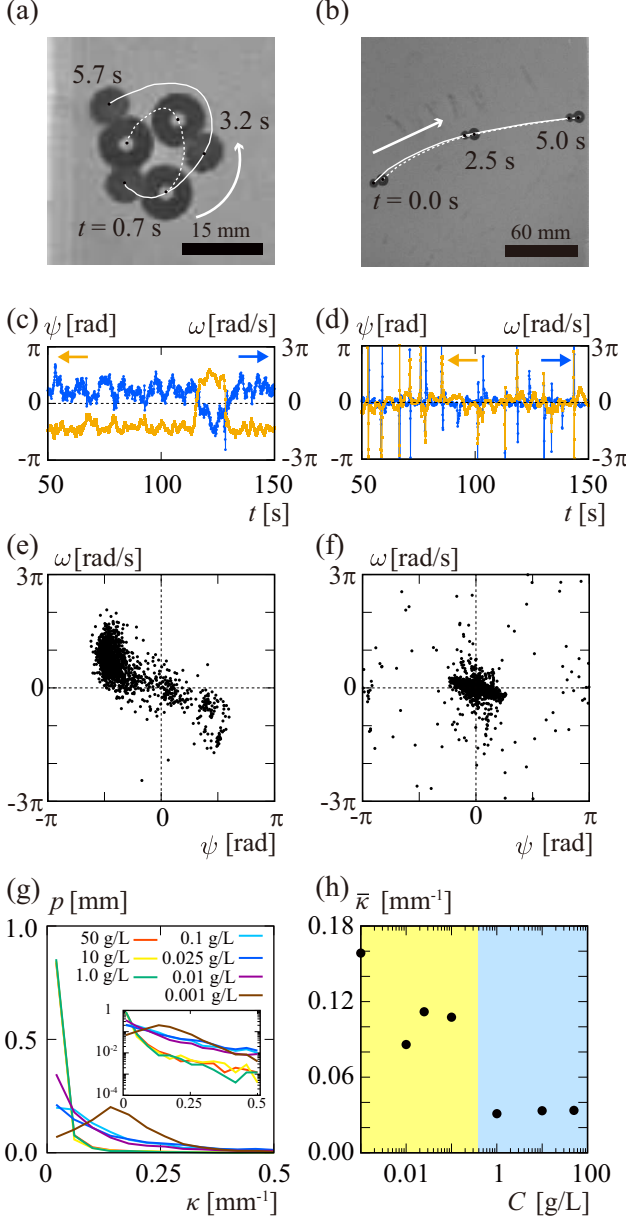


FIG. 2. (a, b) Superimposed images of the camphor disk and metal washer, whose trajectories are denoted as solid and dotted lines, respectively. (a) Circular and (b) straight motions observed on the PEG aqueous solutions at $C =$ (a) 0.001 and (b) 10 g/L. (c, d) Time series of the drift angle ψ (orange) and angular velocity ω (blue) for (c) circular and (d) straight motions. t corresponds to those in (a) and (b). (e, f) Relationship between the drift angle ψ and the angular velocity ω for (e) circular and (f) straight motions. (g) Distribution p on unsigned curvature κ of the camphor disk trajectory. The inset shows the semi-logarithmic plot. (h) $\bar{\kappa}$ based on the PEG concentration C . The yellow and light blue areas represent the circular and straight motions, respectively.

as

$$\frac{\partial u}{\partial t} = D\Delta u - \alpha u + G(\mathbf{r}, \mathbf{r}_s). \quad (1)$$

Here, D is the effective diffusion coefficient [31, 32], and α is the sublimation rate of the surface-active molecules. $G(\mathbf{r}, \mathbf{r}_s)$ represents the supply rate of the molecules from the source particle located at \mathbf{r}_s ,

$$G(\mathbf{r}, \mathbf{r}_s) = \frac{G_0}{S_0} H_\epsilon(\mathbf{r}, \mathbf{r}_s, R_s), \quad (2)$$

where R_s and S_0 denote the radius and area of the source particle, respectively. G_0 is the total supply rate of the surface-active molecules. H_ϵ is the smoothed step function defined as

$$H_\epsilon(\mathbf{r}, \mathbf{r}', R') = \frac{1}{2} \left(1 + \tanh \frac{R' - |\mathbf{r} - \mathbf{r}'|}{\epsilon} \right). \quad (3)$$

Here, ϵ is a small positive parameter for smoothing. When $\epsilon \rightarrow +0$, the function $H_\epsilon(\mathbf{r}, \mathbf{r}', R')$ is replaced with a step function as

$$H_0(\mathbf{r}, \mathbf{r}', R') = \begin{cases} 1, & |\mathbf{r} - \mathbf{r}'| \leq R', \\ 0, & |\mathbf{r} - \mathbf{r}'| > R'. \end{cases} \quad (4)$$

The dynamics for the motion of the source and inert particles are described as

$$m_s \frac{d^2 \mathbf{r}_s}{dt^2} = -\eta_s \frac{d\mathbf{r}_s}{dt} + \mathbf{F}_{\text{conc}}(\gamma, \mathbf{r}, \mathbf{r}_s, R_s) + \mathbf{F}_{\text{int}}(\mathbf{r}_i - \mathbf{r}_s), \quad (5)$$

and

$$m_i \frac{d^2 \mathbf{r}_i}{dt^2} = -\eta_i \frac{d\mathbf{r}_i}{dt} + \mathbf{F}_{\text{conc}}(\gamma, \mathbf{r}, \mathbf{r}_i, R_i) + \mathbf{F}_{\text{int}}(\mathbf{r}_s - \mathbf{r}_i), \quad (6)$$

where m_s and η_s denote the mass and viscous resistance coefficient for the source particle, respectively, while m_i and η_i denote the mass and viscous resistance coefficient for the inert particle, respectively.

The force originating from the surface tension gradient, \mathbf{F}_{conc} , is defined as

$$\mathbf{F}_{\text{conc}}(\gamma, \mathbf{r}, \mathbf{r}', R') = \iint_{\mathbb{R}^2} [\nabla \gamma] H_\epsilon(\mathbf{r}, \mathbf{r}', R') d\mathbf{r}, \quad (7)$$

which is illustrated in Fig. 3(a). It should be noted that

$$\iint_{\mathbb{R}^2} [\nabla \gamma] H_0(\mathbf{r}, \mathbf{r}', R') d\mathbf{r} = \int_{\partial\Omega} \gamma \mathbf{n}(\mathbf{r}') dl', \quad (8)$$

holds when $\epsilon \rightarrow +0$. Here, $\partial\Omega$ is the periphery of the particle, and dl' is a line element along it. $\mathbf{n}(\mathbf{r}')$ is a unit normal vector directing outward from the particle at the periphery. The expression in Eq. (8) shows that \mathbf{F}_{conc}

represents the summation of the surface tension exerting perpendicular at the periphery of the particle.

Here, we assume the following linear relationship between the surface tension γ and concentration u :

$$\gamma = \gamma_0 - \Gamma u, \quad (9)$$

where γ_0 is the surface tension of the camphor-free aqueous phase. Γ is a positive constant, reflecting that surface-active molecules decrease the surface tension of the aqueous phase [32, 33].

The force \mathbf{F}_{int} is defined as

$$\mathbf{F}_{\text{int}}(\mathbf{l}) = F_{\text{int}}(|\mathbf{l}|) \frac{\mathbf{l}}{|\mathbf{l}|} = \begin{cases} f\mathcal{K}_1(q|\mathbf{l}|) \frac{\mathbf{l}}{|\mathbf{l}|}, & |\mathbf{l}| > R_s + R_i, \\ (a|\mathbf{l}| + b) \frac{\mathbf{l}}{|\mathbf{l}|}, & |\mathbf{l}| \leq R_s + R_i, \end{cases} \quad (10)$$

which describes the attractive lateral capillary force [29] and short-range exclusive volume effect between the particles for $|\mathbf{l}| > R_s + R_i$ and $|\mathbf{l}| < R_s + R_i$, respectively (Fig 3(b)). Here, \mathbf{l} is the relative position vector from the considered particle to the other particle. \mathcal{K}_1 is the modified Bessel function of the second kind of order 1, and q is the inverse of the capillary length. The constant b is explicitly described as

$$b = f\mathcal{K}_1(q(R_s + R_i)) - (R_s + R_i)a, \quad (11)$$

where a is an effective spring constant, which is related to the excluded volume. The surface tension modulation caused by camphor molecules, Γ , is negligible and thus we can neglect the dependence of the lateral capillary force on the concentration u . For simplicity, we set $m_s = m_i = m$, $\eta_s = \eta_i = \eta$, and $R_s = R_i = R$.

In numerical calculations and theoretical analyses, we adopt the dimensionless form of the model. The dimensionless variables and coefficients are defined as

$$\begin{aligned} \tilde{t} &= \alpha t, & \tilde{\mathbf{r}} &= \sqrt{\frac{\alpha}{D}} \mathbf{r}, & \tilde{q} &= \sqrt{\frac{D}{\alpha}} q, & \tilde{\mathbf{l}} &= \sqrt{\frac{\alpha}{D}} \mathbf{l}, \\ \tilde{G}_0 &= \frac{1}{\alpha S_0 u_0} G_0, & \tilde{\eta} &= \frac{1}{m\alpha} \eta, & \tilde{\Gamma} &= \frac{u_0}{m\alpha^2} \Gamma, \\ \tilde{f} &= \frac{1}{m\alpha\sqrt{D\alpha}} f, & \tilde{R} &= \sqrt{\frac{\alpha}{D}} R, & \tilde{\epsilon} &= \sqrt{\frac{\alpha}{D}} \epsilon, \\ \tilde{a} &= \frac{1}{m\alpha^2} a, & \tilde{b} &= \frac{1}{m\alpha\sqrt{D\alpha}} b, & \tilde{u} &= \frac{u}{u_0}. \end{aligned} \quad (12)$$

Here u_0 is the unit of concentration. The tildes (\sim) are omitted hereafter for simplicity. The dimensionless forms

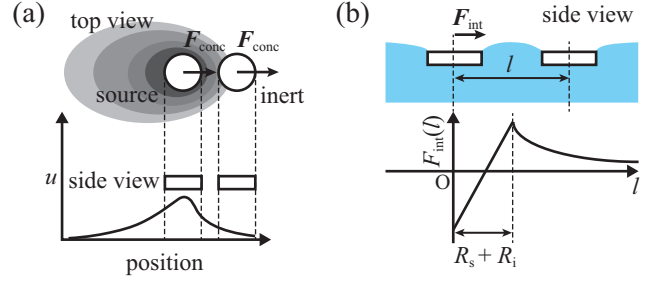


FIG. 3. Force applied to the particle. (a) Force originating from the concentration field. (b) Profile of attractive lateral capillary force and repulsive force owing to the short-range exclusive volume effect. The graph shows the force applied to the particle at the origin from another particle at $l = |\mathbf{l}|$ away.

are summarized as

$$\frac{\partial u}{\partial t} = \Delta u - u + G_0 H_\epsilon(\mathbf{r}, \mathbf{r}_s, R), \quad (13)$$

$$\begin{aligned} \frac{d^2 \mathbf{r}_s}{dt^2} &= -\eta \frac{d\mathbf{r}_s}{dt} - \Gamma \iint_{\mathbb{R}^2} [\nabla u] H_\epsilon(\mathbf{r}, \mathbf{r}_s, R) d\mathbf{r} \\ &\quad + \mathbf{F}_{\text{int}}(\mathbf{r}_i - \mathbf{r}_s), \end{aligned} \quad (14)$$

$$\begin{aligned} \frac{d^2 \mathbf{r}_i}{dt^2} &= -\eta \frac{d\mathbf{r}_i}{dt} - \Gamma \iint_{\mathbb{R}^2} [\nabla u] H_\epsilon(\mathbf{r}, \mathbf{r}_i, R) d\mathbf{r} \\ &\quad + \mathbf{F}_{\text{int}}(\mathbf{r}_s - \mathbf{r}_i), \end{aligned} \quad (15)$$

$$H_\epsilon(\mathbf{r}, \mathbf{r}', R') = \frac{1}{2} \left(1 + \tanh \frac{R' - |\mathbf{r} - \mathbf{r}'|}{\epsilon} \right), \quad (16)$$

$$\mathbf{F}_{\text{int}}(\mathbf{l}) = \begin{cases} f\mathcal{K}_1(q|\mathbf{l}|) \frac{\mathbf{l}}{|\mathbf{l}|}, & |\mathbf{l}| > 2R, \\ (a|\mathbf{l}| + b) \frac{\mathbf{l}}{|\mathbf{l}|}, & |\mathbf{l}| \leq 2R, \end{cases} \quad (17)$$

$$b = f\mathcal{K}_1(2Rq) - 2Ra. \quad (18)$$

Numerical calculations were performed by changing η and Γ as parameters. Γ represents the intensity of the driving force. The other parameters were $a = 40$, $G_0 = 4/\pi$, $q = 0.7$, $f = 0.1$, $R = 0.5$, and $\epsilon = 0.1$.

The concentration field was calculated using the alternating direction implicit (ADI) method [34], and the positions of the source and inert particles were integrated using the Euler method. We adopted a periodic boundary condition to investigate the long-term behavior without the effect of the finite system size. The system size, time step, and spatial mesh were $L = 25.6$, $\Delta t = 0.005$, and $\Delta x = 0.1$, respectively. The initial position of the inert particle was set at the center of the calculation area, and the initial position of the source particle was set at the angles of $\pi/9$, $2\pi/9$, and $\pi/3$ from the x -axis with a distance of $1/q$ from the inert particle to check whether the effect of anisotropy on the spatial mesh configuration can be neglected. The initial velocity of the inert particle was 0, and the initial velocity of the source particle was set in the opposite direction to the inert particle with an absolute value of 0.01.

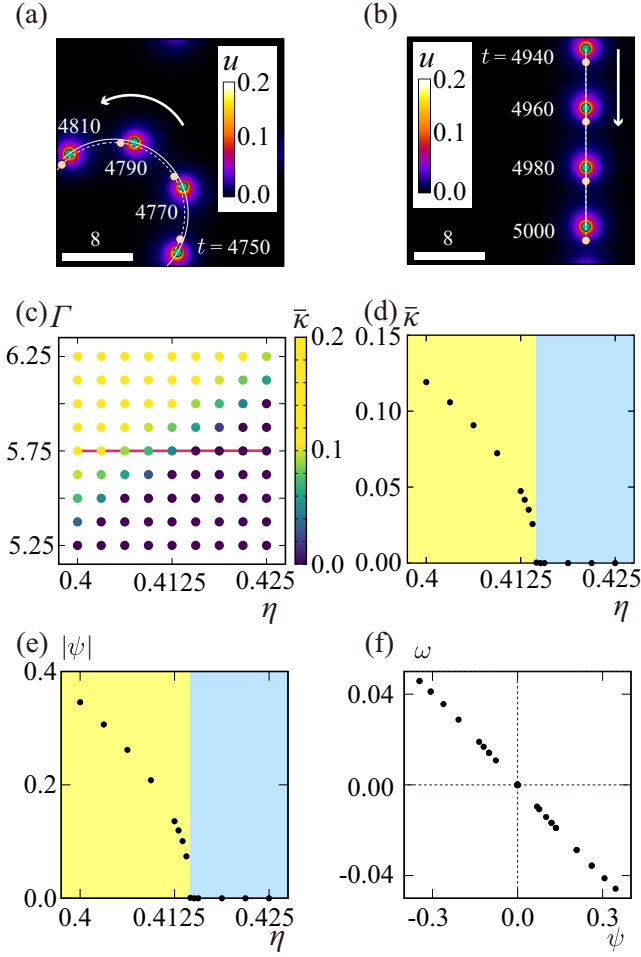


FIG. 4. (a, b) Superimposed images obtained using numerical calculations, in which the color map shows the profile of u . The green and pink disks represent the source and inert particles, respectively. The solid and dotted lines exhibit trajectories of the source and inert particles, respectively. The white arrows indicate the direction of motions. (a) Circular motion for $\Gamma = 5.75$ and $\eta = 0.4$. (b) Straight motion for $\Gamma = 5.75$ and $\eta = 0.425$. (c) Phase diagram that classifies circular and straight motions based on the mean value of the unsigned curvature, $\bar{\kappa}$, on the Γ - η plane. The source and inert particles exhibited circular motion for higher Γ and lower η , while they exhibited the straight motion for lower Γ and higher η . (d) Dependence of $\bar{\kappa}$ on η for fixed $\Gamma = 5.75$ on the red line in (c). (e) Dependence of $|\psi|$ on η for fixed $\Gamma = 5.75$ on the red line in (c). The yellow and light blue areas represent the parameter regions where circular and straight motions appeared, respectively in (d) and (e). (f) Relationship between the drift angle ψ and angular velocity ω .

The pair of the source and inert particles exhibited steady motion after a long time. The superimposed images obtained based on the numerical calculation are shown in Figs. 4(a) and (b), in which the profile of the concentration field u and the position of the source and inert particles are displayed. The trajectories of the source and inert particles are denoted as solid and dot-

ted lines, respectively. They exhibited a straight motion for higher η and lower Γ , and they exhibited a circular motion for smaller η and larger Γ . In both the cases, the inert particle was in the front side, while the source particle was in the rear side. To discuss the transition between the straight and circular motions, the unsigned curvature of the trajectory of the source particle was evaluated. We confirmed that the unsigned curvature of the trajectory reached a steady value, and the values were almost the same independent of the initial condition for the particles configuration. Figure 4(c) shows the phase diagram, in which the mean value of the unsigned curvature $\bar{\kappa}$ is shown. To obtain $\bar{\kappa}$, the time average between $t = 225$ and $t = 250$ was considered for each initial condition, and the mean value of the data for three different initial conditions for the particle configuration was obtained. The smaller $\bar{\kappa}$ indicates the straight motion, while the larger $\bar{\kappa}$ indicates the circular motion. That is to say, when Γ was larger and η was smaller, they exhibited a circular motion. In contrast, when Γ was smaller and η was larger, they exhibited a straight motion. The transition shown in Fig. 4(d) corresponds to the experimental observation in Fig. 2(h). Figure 4(e) shows the absolute value of the drift angle ψ . The transition of $|\psi|$ occurs at the same value of η as that of $\bar{\kappa}$. When the source and inert particles exhibit circular motions, the drift angle ψ possesses the opposite sign to the angular velocity ω (Fig. 4(f)). It implies that the inert particle rotated with a smaller radius than the source particle. These numerical results qualitatively agree with the experimental results.

IV. BIFURCATION ANALYSIS

To elucidate the transition between the circular and straight pairing-induced motions of the source and inert particles, we perform the linear stability analysis for the straight motion at a constant velocity (Fig. 5(a)) and discuss the transition based on the bifurcation theory.

Considering that the linearity of the evolution equation in Eq. (1) except for the source term, the concentration field u of the surface-active molecules that spread from the source particle can be described as a functional of the source particle position $\mathbf{r}_s(t)$. For the analyses, we adopt the approximation that the concentration field u is represented as a function of the relative position $\mathbf{r} - \mathbf{r}_s$ and the velocity of the source particle $\mathbf{v}_s = d\mathbf{r}_s/dt$. That is to say, the concentration field is represented as

$$u(\mathbf{r}) = u_v(\mathbf{r} - \mathbf{r}_s, \mathbf{v}_s), \quad (19)$$

whose representative profile with $\mathbf{r}_s = \mathbf{0}$ and $\mathbf{v}_s = \mathbf{e}_x$ is shown in Fig. 5(b). The exact solution of $u_v(\mathbf{r}, \mathbf{v})$ is obtained in the form of infinite series, whose explicit expression together with the brief derivation is shown in Appendix. This concentration field exerts the force on the source or inert particle with a radius of R located at

\mathbf{r}' as

$$\begin{aligned}\mathbf{F} &= -\Gamma \iint_{\mathbb{R}^2} \nabla u_v(\mathbf{r} - \mathbf{r}_s, \mathbf{v}_s) H_0(\mathbf{r}, \mathbf{r}', R) d\mathbf{r} \\ &= -\Gamma \iint_{\mathbb{R}^2} \nabla u_v(\mathbf{r}, \mathbf{v}_s) H_0(\mathbf{r}, \mathbf{r}' - \mathbf{r}_s, R) d\mathbf{r} \\ &\equiv \mathbf{F}_v(\mathbf{r}' - \mathbf{r}_s, \mathbf{v}_s, R).\end{aligned}\quad (20)$$

Thus, the force working on the particle through the concentration field is represented by \mathbf{F}_v , which is a function of the relative position of the focused particle from the source particle and the velocity of the source particle. Owing to this approximation, our original system comprised the partial differential equation (PDE) for the concentration field and ordinary differential equations (ODEs) for the particle position is simplified into the system described by the two second-order ODEs for \mathbf{r}_s and \mathbf{r}_i .

We discuss the linear stability of the straight pairing-induced motion. Our system is now expressed as an autonomous dynamical system with the eight degrees of freedom, i.e., \mathbf{r}_s , \mathbf{r}_i , $\mathbf{v}_s = d\mathbf{r}_s/dt$, and $\mathbf{v}_i = d\mathbf{r}_i/dt$. For the analysis, we introduce the position of the COM $\mathbf{r} = (\mathbf{r}_s + \mathbf{r}_i)/2$ and the relative position $\boldsymbol{\ell} = \mathbf{r}_i - \mathbf{r}_s$ in the place of \mathbf{r}_s and \mathbf{r}_i . The velocity of the COM and relative velocity are introduced as $\mathbf{v} = (\mathbf{v}_s + \mathbf{v}_i)/2$ and $\mathbf{w} = \mathbf{v}_i - \mathbf{v}_s$, respectively. Our simplified dynamical system based on \mathbf{r} , $\boldsymbol{\ell}$, \mathbf{v} , and \mathbf{w} is explicitly described as

$$\frac{d\mathbf{r}}{dt} = \mathbf{v}, \quad (21)$$

$$\begin{aligned}\frac{d\mathbf{v}}{dt} &= -\eta\mathbf{v} + \frac{1}{2} \left[\mathbf{F}_v\left(\mathbf{0}, \mathbf{v} - \frac{1}{2}\mathbf{w}, R\right) \right. \\ &\quad \left. + \mathbf{F}_v\left(\boldsymbol{\ell}, \mathbf{v} - \frac{1}{2}\mathbf{w}, R\right) \right],\end{aligned}\quad (22)$$

$$\frac{d\boldsymbol{\ell}}{dt} = \mathbf{w}, \quad (23)$$

$$\begin{aligned}\frac{d\mathbf{w}}{dt} &= -\eta\mathbf{w} - \mathbf{F}_v\left(\mathbf{0}, \mathbf{v} - \frac{1}{2}\mathbf{w}, R\right) \\ &\quad + \mathbf{F}_v\left(\boldsymbol{\ell}, \mathbf{v} - \frac{1}{2}\mathbf{w}, R\right) - 2\mathbf{F}_{\text{int}}(\boldsymbol{\ell}).\end{aligned}\quad (24)$$

First, we construct the solution corresponding to the straight pairing-induced motion in the positive x direction. Considering that the inert particle precedes in the straight pairing-induced motion, as shown in Fig. 5(a), the solution is described using a constant speed v_0 and a constant interval ℓ_0 as

$$\mathbf{r}(t) = v_0 t \mathbf{e}_x, \quad (25)$$

$$\mathbf{v}(t) = v_0 \mathbf{e}_x, \quad (26)$$

$$\boldsymbol{\ell}(t) = \ell_0 \mathbf{e}_x, \quad (27)$$

$$\mathbf{w}(t) = \mathbf{0}, \quad (28)$$

The constant speed v_0 and ℓ_0 should be determined, so that the two relations related to the force balance in the x direction,

$$-2\eta v_0 \mathbf{e}_x + \mathbf{F}_v(\mathbf{0}, v_0 \mathbf{e}_x, R) + \mathbf{F}_v(\ell_0 \mathbf{e}_x, v_0 \mathbf{e}_x, R) = \mathbf{0}, \quad (29)$$

and

$$-\mathbf{F}_v(\mathbf{0}, v_0 \mathbf{e}_x, R) + \mathbf{F}_v(\ell_0 \mathbf{e}_x, v_0 \mathbf{e}_x, R) - 2\mathbf{F}_{\text{int}}(\ell_0 \mathbf{e}_x) = \mathbf{0}, \quad (30)$$

should hold.

The perturbation for the linear stability analysis is described as

$$\mathbf{r}(t) = v_0 t \mathbf{e}_x + \delta \mathbf{r}(t) = v_0 t \mathbf{e}_x + \delta r_x(t) \mathbf{e}_x + \delta r_y(t) \mathbf{e}_y, \quad (31)$$

$$\mathbf{v}(t) = v_0 \mathbf{e}_x + \delta \mathbf{v}(t) = v_0 \mathbf{e}_x + \delta v_x(t) \mathbf{e}_x + \delta v_y(t) \mathbf{e}_y, \quad (32)$$

$$\boldsymbol{\ell}(t) = \ell_0 \mathbf{e}_x + \delta \boldsymbol{\ell}(t) = \ell_0 \mathbf{e}_x + \delta \ell_x(t) \mathbf{e}_x + \delta \ell_y(t) \mathbf{e}_y, \quad (33)$$

$$\mathbf{w}(t) = \delta \mathbf{w}(t) = \delta w_x(t) \mathbf{e}_x + \delta w_y(t) \mathbf{e}_y. \quad (34)$$

The linearized equations are separated into two independent parts

$$\frac{d}{dt} \begin{pmatrix} \delta \ell_x \\ \delta v_x \\ \delta w_x \end{pmatrix} = A_x \begin{pmatrix} \delta \ell_x \\ \delta v_x \\ \delta w_x \end{pmatrix}, \quad (35)$$

$$\frac{d}{dt} \begin{pmatrix} \delta \ell_y \\ \delta v_y \\ \delta w_y \end{pmatrix} = A_y \begin{pmatrix} \delta \ell_y \\ \delta v_y \\ \delta w_y \end{pmatrix}, \quad (36)$$

and a slave equation,

$$\frac{d}{dt} \delta \mathbf{r} = \delta \mathbf{v}, \quad (37)$$

where A_i ($i = x, y$) is explicitly described as

$$A_i = \begin{pmatrix} 0 & 0 & 1 \\ \frac{f_i}{2} & -\eta + \frac{g_i + h_i}{2} & -\frac{g_i + h_i}{4} \\ f_i - 2p_i & g_i - h_i & -\eta - \frac{g_i - h_i}{2} \end{pmatrix}. \quad (38)$$

To obtain the aforementioned linearized equation, we used the relation in Eqs. (29) and (30). Here, f_i , g_i , h_i , and p_i are defined as

$$f_i = \lim_{\varepsilon \rightarrow 0} \frac{1}{\varepsilon} [\mathbf{F}_v(\ell_0 \mathbf{e}_x + \varepsilon \mathbf{e}_i, v_0 \mathbf{e}_x, R) - \mathbf{F}_v(\ell_0 \mathbf{e}_x, v_0 \mathbf{e}_x, R)] \cdot \mathbf{e}_i, \quad (39)$$

$$g_i = \lim_{\varepsilon \rightarrow 0} \frac{1}{\varepsilon} [\mathbf{F}_v(\ell_0 \mathbf{e}_x, v_0 \mathbf{e}_x + \varepsilon \mathbf{e}_i, R) - \mathbf{F}_v(\ell_0 \mathbf{e}_x, v_0 \mathbf{e}_x, R)] \cdot \mathbf{e}_i, \quad (40)$$

$$h_i = \lim_{\varepsilon \rightarrow 0} \frac{1}{\varepsilon} [\mathbf{F}_v(\mathbf{0}, v_0 \mathbf{e}_x + \varepsilon \mathbf{e}_i, R) - \mathbf{F}_v(\mathbf{0}, v_0 \mathbf{e}_x, R)] \cdot \mathbf{e}_i, \quad (41)$$

$$p_i = \lim_{\varepsilon \rightarrow 0} \frac{1}{\varepsilon} [\mathbf{F}_{\text{int}}(\ell_0 \mathbf{e}_x + \varepsilon \mathbf{e}_i) - \mathbf{F}_{\text{int}}(\ell_0 \mathbf{e}_x)] \cdot \mathbf{e}_i. \quad (42)$$

Eigenvalues are obtained as the solution of the characteristic polynomial of A_i ,

$$\lambda^3 + (2\eta - h_i)\lambda^2 + (\eta^2 - h_i\eta + 2p_i - f_i)\lambda + (2p_i - f_i)\eta - (g_i + h_i)p_i + f_i h_i = 0. \quad (43)$$

Here, we consider the isotropy of the system, i.e., the solution in which the straight pairing-induced motion in any direction should exist. Therefore, Eqs. (29) and Eqs. (30) hold if we substitute $v_0(\cos \nu \mathbf{e}_x + \sin \nu \mathbf{e}_y)$ and $\ell_0(\cos \nu \mathbf{e}_x + \sin \nu \mathbf{e}_y)$ for $v_0 \mathbf{e}_x$ and $\ell_0 \mathbf{e}_x$, respectively, where ν is a small parameter. Up to the first order of ν , we obtain

$$(2p_y - f_y)\eta - p_y(g_y + h_y) + f_y h_y = 0. \quad (44)$$

Therefore, the characteristic polynomial for A_y is simplified as

$$\lambda [\lambda^2 + (2\eta - h_y)\lambda + \eta^2 - h_y\eta + 2p_y - f_y] = 0. \quad (45)$$

That is to say, the matrix A_y possesses a zero eigenvalue, and the corresponding eigenvector is $^t(\ell_0, v_0, 0)$.

Using the aforementioned equations, we investigated the linear stability by adopting parameter values that were used in the numerical calculation. In the numerical evaluation, we truncated the infinite series of u_v in Eq. (A.6) till $n = 10$. The limits of ε in Eqs. (39)–(42) were calculated by setting $\varepsilon = 10^{-3}$. For both approximations, we confirmed that the accuracy was within 10^{-3} .

For the evaluation, we first numerically obtained v_0 and ℓ_0 for η and Γ based on Eqs. (29) and (30). We used the values which satisfied the equations with the accuracy of 10^{-3} . The obtained values of v_0 are plotted against η with constant $\Gamma = 5.75$ in Fig. 5(c), and those for ℓ_0 in Fig. 5(d). v_0 decreased with an increase in η , while ℓ_0 increased with an increase in η .

Using the obtained values of v_0 and ℓ_0 , we calculated f_i , g_i , h_i , and p_i ($i = x, y$), and then calculated the eigenvalues of A_x and A_y using Eqs. (43) and (45), respectively. The real parts of the eigenvalues of A_x are plotted against η in Fig. 5(e), while those of A_y are plotted against η in Fig. 5(f). It should be noted that the zero eigenvalue is not shown in Fig. 5(f). As shown in Fig. 5(e), the straight pairing-induced motion with a translational speed v_0 at a distance of ℓ_0 between the

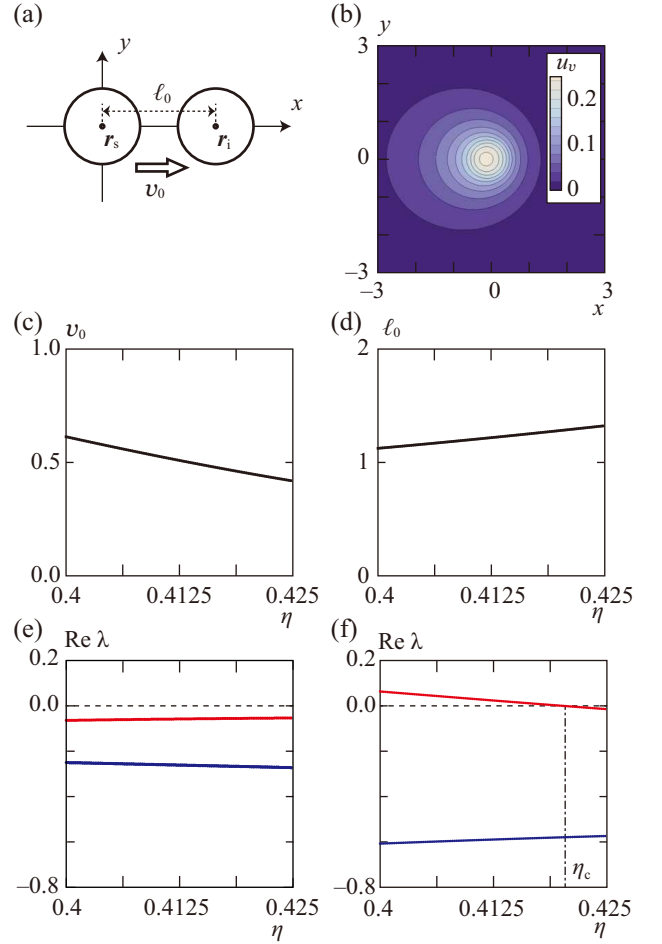


FIG. 5. (a) Coordinate system and straight pairing-induced motion. (b) Representative profile of $u_v(\mathbf{r}, \mathbf{v}_s)$, where $\mathbf{v}_s = \mathbf{e}_x$. The contours at every interval of 0.2 are shown. (c) v_0 against η for $\Gamma = 5.75$. (d) ℓ_0 against η for $\Gamma = 5.75$. (e) Real parts of eigenvalues λ of A_x calculated for each η . The eigenvalue around $\text{Re } \lambda \simeq -0.05$ (plotted with red) is real, while other eigenvalues around $\text{Re } \lambda \simeq -0.25$ (plotted with blue) are complex. (f) Real parts of the eigenvalues λ of A_y calculated for each η . The zero eigenvalue is not plotted.

two particle is stable as far as the perturbation in the x -axis direction is concerned. As shown in Fig. 5(f), the maximum real parts of the eigenvalues of A_y changed its sign at $\eta = \eta_c \simeq 0.42$. This means that the straight pairing-induced motion is stable for $\eta > \eta_c$ and unstable for $\eta < \eta_c$. This result qualitatively agrees with numerical results, though the threshold value is slightly greater in the theoretical analysis. Considering that the eigenvalue whose real part changes its sign at $\eta = \eta_c$ does not have an imaginary part, and that the system is symmetric with the x -axis, the transition between the circular and straight pairing-induced motions is most likely classified as a pitchfork bifurcation. As higher-order terms are not calculated, we cannot distinguish whether the bifurcation is supercritical or subcritical. Based on the numerical results shown in Figs. 4 (d) and (e), the bifurcation is

supposed to be a supercritical pitchfork bifurcation.

V. CONCLUSION

In this study, we focus on the pairing-induced motion of the source and inert particles. In the experiments, we used the camphor disk and metal washer as the source and inert particles, respectively. After we floated them on PEG aqueous solution, they attracted each other through the attractive lateral capillary force. Then, they showed circular and straight motions on the aqueous solution with lower and higher PEG concentration, respectively. We constructed a mathematical model to discuss the transition between the circular and straight motions. In the model, we considered time developments for the positions of the source particle, inert particle, and concentration field formed by the source particle. In numerical calculations, we reproduced circular and straight motions corresponding to the experimental results. Furthermore, we performed the linear stability analysis based on the straight pairing-induced motion and the obtained results were quantitatively consistent with the numerical results. The analysis suggested that the transition can be understood in terms of the pitchfork bifurcation.

In the current analysis, the force originating from the concentration fields, \mathbf{F}_v , is approximated by taking up to the first-order terms with respect to time derivative of the source particle position. This expression of the force is exact when the source particle moves at a uniform velocity, and it enabled us to discuss the transition between the straight and circular motions. Indeed, we did not observe such transition when the concentration field is represented as the function of the relative position as mentioned in the previous study [15]. We expect that further complex dynamics such as zig-zag, quasi-periodic, and chaotic motions [35] can be realized by adequately choosing experimental conditions and/or numerical parameters. To address such complicated motions based on the bifurcation analysis, we need to improve our analysis method. One possible candidate is to include higher-order terms in the expansion of the concentration field with respect to the velocity, acceleration, jerk, and combination of these terms [36–38].

We should bear in mind that the effective interaction induced by concentration fields is non-reciprocal, i.e., it breaks the action-reaction law. Experimentally, a single camphor disk shows self-propulsion in the absence of a washer. However, numerically and theoretically, a pair of source and inert particles can have self-propulsion even in the parameter range where a single source particle cannot have self-propulsion. The pair-induced motion is a direct consequence of the non-reciprocal interaction, and our study describes the relevance of its dynamic aspect. The well-known camphor-water system should be re-investigated based on the new perspective of non-reciprocal interaction [39–41].

One can easily conceive the extension of the present

system to one with multiple particles. The collective motion of particles driven by the dynamics of the concentration field has not yet been understood in detail. The knowledge drawn from our study can be applied to develop experimental and numerical systems. The expansion of the concentration field as used in the present study can be adopted to construct simple models with multiple particles by extracting the essential dynamics of the concentration field. We believe that the possibility of extracting complex motions from such a simple system will lead to a better understanding of the collective motions of migrating cells and bacteria.

ACKNOWLEDGMENTS

The authors acknowledge Professor Jerzy Gorecki (Polish Academy of Sciences), Professor Hiroaki Ito (Chiba University), and Professor Masaharu Nagayama (Hokkaido University) for their fruitful discussion. This study was supported by JSPS KAKENHI Grant Nos. JP19J00365, JP19H05403, JP20K14370, JP20H02712, JP21H00409, JP21H00996, and JP21H01004 and the Cooperative Research Program of “Network Joint Research Center for Materials and Devices: Dynamic Alliance for Open Innovation Bridging Human, Environment and Materials” (Nos. 20211014 and 20214004). Furthermore, this study was supported by JSPS and PAN under the Japan-Poland Research Cooperative Program (No. JPJSBP120204602).

Appendix: Derivation of u_v

In this Appendix, we derive the concentration field $u_v(\mathbf{r}, \mathbf{v})$ generated by the source particle whose position and velocity are $\mathbf{0}$ and \mathbf{v} , respectively. We consider the situation that the source particle moves at a constant velocity $\mathbf{V} = V\mathbf{e}_x$. We introduce the co-moving frame $\boldsymbol{\rho}$, in which the source particle is located at the origin. The dynamics for the concentration field is described as

$$\frac{\partial u}{\partial t} - V\mathbf{e}_x \cdot \nabla u = \Delta u - u + G_0 H_0(\boldsymbol{\rho}, \mathbf{0}, R). \quad (\text{A.1})$$

The stationary solution $U(\boldsymbol{\rho}; V)$ should satisfy

$$-V\mathbf{e}_x \cdot \nabla U = \Delta U - U + G_0 H_0(\boldsymbol{\rho}, \mathbf{0}, R). \quad (\text{A.2})$$

The general solution of the homogeneous equation for Eq. (A.2)

$$-V\mathbf{e}_x \cdot \nabla U = \Delta U - U, \quad (\text{A.3})$$

is given as the linear combination of

$$U(\rho, \phi; V) = \mathcal{I}_n(k\rho) \exp(-\rho\mu \cos \phi) \exp(in\phi), \quad (\text{A.4})$$

and

$$U(\rho, \phi; V) = \mathcal{K}_n(k\rho) \exp(-\rho\mu \cos \phi) \exp(in\phi), \quad (\text{A.5})$$

in the polar coordinates ρ and ϕ , which satisfy $\boldsymbol{\rho} = \rho(\cos\phi\mathbf{e}_x + \sin\phi\mathbf{e}_y)$ [42]. Here, n is an integer, $k = \sqrt{1+V^2/4}$, and $\mu = V/2$. \mathcal{I}_n and \mathcal{K}_n are the modified Bessel functions of the first and second kinds of order n , respectively. Therefore, the solution of Eq. (A.2) is obtained as

$$U(\boldsymbol{\rho}; V) = \begin{cases} G_0 - G_0 \sum_{n=0}^{\infty} \alpha_n \mathcal{I}_n(k\rho) \exp(-\rho\mu \cos\phi) \cos n\phi, & \rho \leq R, \\ G_0 \sum_{n=0}^{\infty} \beta_n \mathcal{K}_n(k\rho) \exp(-\rho\mu \cos\phi) \cos n\phi, & \rho > R. \end{cases} \quad (\text{A.6})$$

Here, the coefficients α_n and β_n are obtained from the continuity condition of U and ∇U at the periphery of the

particle. They are explicitly given as

$$\alpha_n = \zeta_n [-kR\mathcal{I}_n(\mu R)\mathcal{K}'_n(kR) + \mu R\mathcal{I}'_n(\mu R)\mathcal{K}_n(kR)], \quad (\text{A.7})$$

$$\beta_n = \zeta_n [kR\mathcal{I}_n(\mu R)\mathcal{I}'_n(kR) - \mu R\mathcal{I}'_n(\mu R)\mathcal{I}_n(kR)], \quad (\text{A.8})$$

where

$$\zeta_n = \begin{cases} 1, & n = 0, \\ 2, & n \geq 1, \end{cases} \quad (\text{A.9})$$

and the prime (') denotes the derivative. When the velocity of the source particle is in the arbitrary direction, the concentration field u_v is obtained as

$$u_v(\mathbf{r}, \mathbf{v}) = U(\mathcal{R}(-\vartheta)\mathbf{r}; |\mathbf{v}|), \quad (\text{A.10})$$

where ϑ holds $\mathbf{v} = |\mathbf{v}|(\cos\vartheta\mathbf{e}_x + \sin\vartheta\mathbf{e}_y)$, where $\mathcal{R}(\vartheta)$ is the rotation matrix

$$\mathcal{R}(\vartheta) = \begin{pmatrix} \cos\vartheta & -\sin\vartheta \\ \sin\vartheta & \cos\vartheta \end{pmatrix}. \quad (\text{A.11})$$

-
- [1] H. Masoud and M. J. Shelley, Phys. Rev. Lett. **112**, 128304 (2014).
[2] V. Vandadi, S. J. Kang, and H. Masoud, J. Fluid Mech. **811**, 612 (2017).
[3] J. L. Anderson, Annu. Rev. Fluid Mech. **21**, 61 (1989).
[4] Z. Izri, M. N. van der Linden, S. Michelin, and O. Dauchot, Phys. Rev. Lett. **113**, 248302 (2014).
[5] S. Yabunaka, T. Ohta, and N. Yoshinaga, J. Chem. Phys. **136**, 074904 (2012).
[6] S. Ramaswamy, Annu. Rev. Condens. Matter Phys. **1**, 323 (2010).
[7] M. C. Marchetti, J. F. Joanny, S. Ramaswamy, T. B. Liverpool, J. Prost, M. Rao, and R. A. Simha, Rev. Mod. Phys. **85**, 1143 (2013).
[8] S. Michelin, E. Lauga, and D. Bartolo, Phys. Fluids **25**, 061701 (2013).
[9] C. Bechinger, R. Di Leonardo, H. Löwen, C. Reichhardt, G. Volpe, and G. Volpe, Rev. Mod. Phys. **88**, 045006 (2016).
[10] T. Vicsek and A. Zafeiris, Phys. Rep. **517**, 71 (2012).
[11] H. Chaté, Annu. Rev. Condens. Matter Phys. **11**, 189 (2020).
[12] A. Nakajima, S. Ishihara, D. Imoto, and S. Sawai, Nat. Commun. **5**, 5367 (2014).
[13] H. C. Berg, *E. coli in Motion* (Springer, 2004).
[14] E. Theveneau, B. Steventon, E. Scarpa, S. Garcia, X. Trepát, A. Streit, and R. Mayor, Nat. Cell. Biol. **15**, 763 (2013).
[15] J. Agudo-Canalejo and R. Golestanian, Phys. Rev. Lett. **123**, 018101 (2019).
[16] M. Nagayama, S. Nakata, Y. Doi, and Y. Hayashima, Physica D **194**, 151 (2004).
[17] Y. Hirose, Y. Yasugahira, M. Okamoto, Y. Koyano, H. Kitahata, M. Nagayama, and Y. Sumino, J. Phys. Soc. Jpn. **89**, 074004 (2020).
[18] Y. Hayashima, M. Nagayama, and S. Nakata, J. Phys. Chem. B **105**, 5353 (2001).
[19] Y. Koyano, T. Sakurai, and H. Kitahata, Phys. Rev. E **94**, 042215 (2016).
[20] C. Tomlinson, Proc. R. Soc. London **11**, 575 (1862).
[21] D. Boniface, C. Cottin-Bizonne, R. Kervil, C. Ybert, and F. Detcheverry, Phys. Rev. E **99**, 062605 (2019).
[22] J. Sharma, I. Tiwari, D. Das, P. Parmananda, V. S. Akella, and V. Pimienta, Phys. Rev. E **99**, 012204 (2019).
[23] H. Morohashi, M. Imai, and T. Toyota, Chem. Phys. Lett. **721**, 104 (2019).
[24] S. Soh, M. Branicki, and B. A. Grzybowski, J. Phys. Chem. Lett. **2**, 770 (2011).
[25] S. Soh, K. J. M. Bishop, and B. A. Grzybowski, J. Phys. Chem. B **112**, 10848 (2008).
[26] H. Nishimori, N. J. Suematsu, and S. Nakata, J. Phys. Soc. Jpn. **86**, 101012 (2017).
[27] O. Schulz and M. Markus, J. Phys. Chem. B **111**, 8175 (2007).
[28] S. Nakata, M. Nagayama, H. Kitahata, N. J. Suematsu, and T. Hasegawa, Phys. Chem. Chem. Phys. **17**, 10326 (2015).
[29] D. Y. C. Chan, J. D. Henry, Jr., and L. R. White, J. Colloid Interface Sci. **79**, 410 (1981).
[30] W. Rasband, *ImageJ* (U. S. National Institutes of Health, Bethesda, Maryland, USA, 1997-2018) <https://imagej.nih.gov/ij/>.
[31] H. Kitahata and N. Yoshinaga, J. Chem. Phys. **148**, 134906 (2018).

- [32] N. J. Suematsu, T. Sasaki, S. Nakata, and H. Kitahata, *Langmuir* **30**, 8101 (2014).
- [33] Y. Karasawa, T. Nomoto, L. Chiari, T. Toyota, and M. Fujinami, *J. Colloid Interface Sci.* **511**, 184 (2018).
- [34] W. H. Press, S. A. Teukolsky, W. T. Vetterling, and B. P. Flannery, *Numerical Recipes in C* (Cambridge University Press, 1992).
- [35] M. Tarama and T. Ohta, *EPL* **114**, 30002 (2016).
- [36] Y. Koyano, T. Sakurai, and H. Kitahata, *Phys. Rev. E* **94**, 042215 (2016).
- [37] Y. Koyano, M. Gryciuk, P. Skrobanska, M. Malecki, Y. Sumino, H. Kitahata, and J. Gorecki, *Phys. Rev. E* **96**, 012609 (2017).
- [38] Y. Koyano, N. J. Suematsu, and H. Kitahata, *Phys. Rev. E* **99**, 022211 (2019).
- [39] N. Cira, A. Benusioglio, and M. Prakash, *Nature* **519**, 446 (2015).
- [40] C. H. Meredith, P. G. Moerman, J. Groenewold, Y.-J. Chiu, W. K. Kegel, A. van Blaaderen, and L. D. Zarzar, *Nat. Chem.* **12**, 1136 (2020).
- [41] M. Fruchart, R. Hanai, P. B. Littlewood, and V. Vitelli, *Nature* **592**, 363 (2021).
- [42] H. Kitahata, Y. Koyano, K. Iida, and M. Nagayama, in *Self-Organized Motion: Physicochemical Design Based on Nonlinear Dynamics*, edited by S. Nakata, V. Pimienta, I. Lagzi, H. Kitahata, and N. J. Suematsu (R. Soc. Chem., Cambridge, 2019).